Supplementary material for: Seismic anisotropy changes across upper mantle phase transitions

Kaiqing Yuan, Caroline Beghein

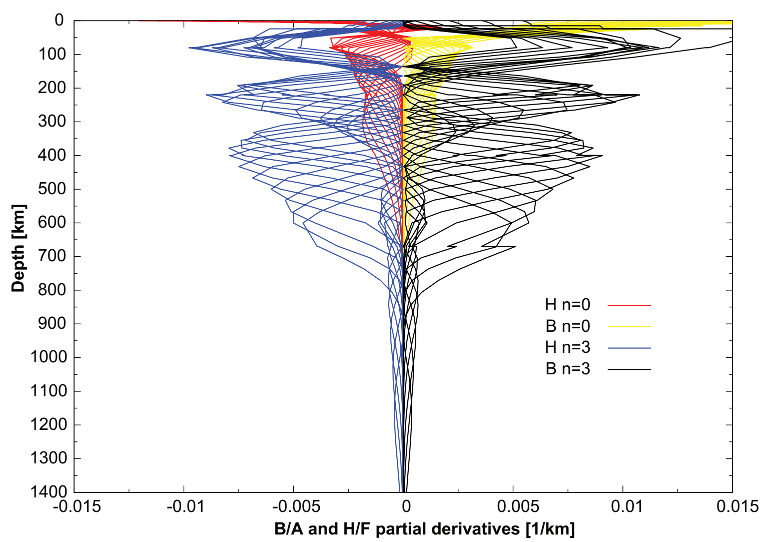

Supplementary Figure 1

Supplementary Figure 1: Depth-dependence of Rayleigh wave phase velocity partial derivatives calculated for perturbations in parameter B and H with respect to P-wave related Love parameters A and F, respectively, using PREM (Dziewonski and Anderson, 1981) for all the fundamental modes and third overtones used in this study. Because the kernels for B and H are almost identical in shape, these two parameters are affected by large trade-offs and cannot be resolved.

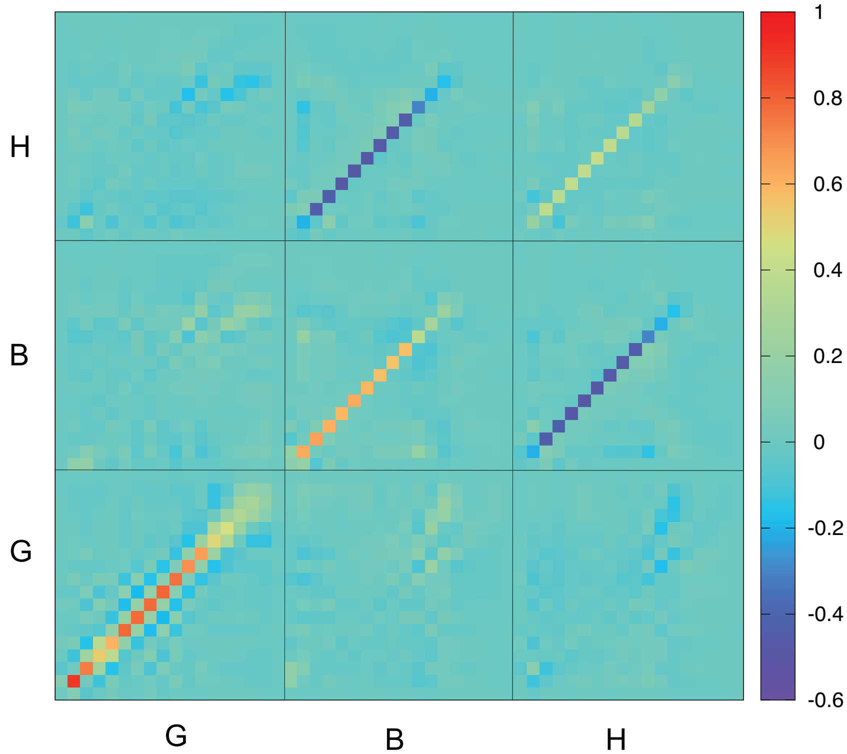

Supplementary Figure 2

Supplementary Figure 2: Resolution matrix showing little trade-offs between G and the other two elastic parameters. Trade-offs between B and H are however well visible.

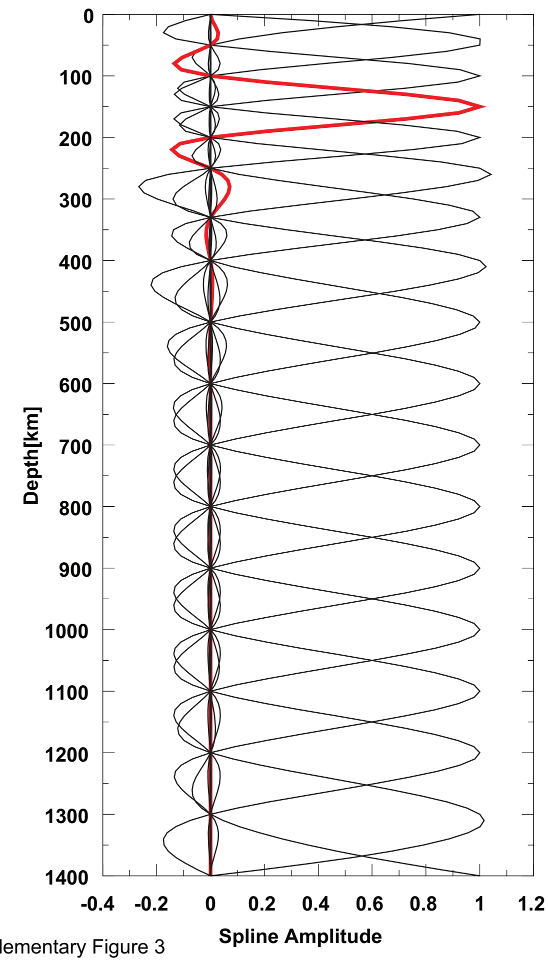

Supplementary Figure 3: Spline functions employed for the depth parametrization. Because Rayleigh wave sensitivity to parameters G_s and G_c is higher in the uppermost mantle, the spacing between splines is smaller at shallower depths than inside and below the transition zone. The red curve highlights one of the splines with peak sensitivity at 250 km depth.

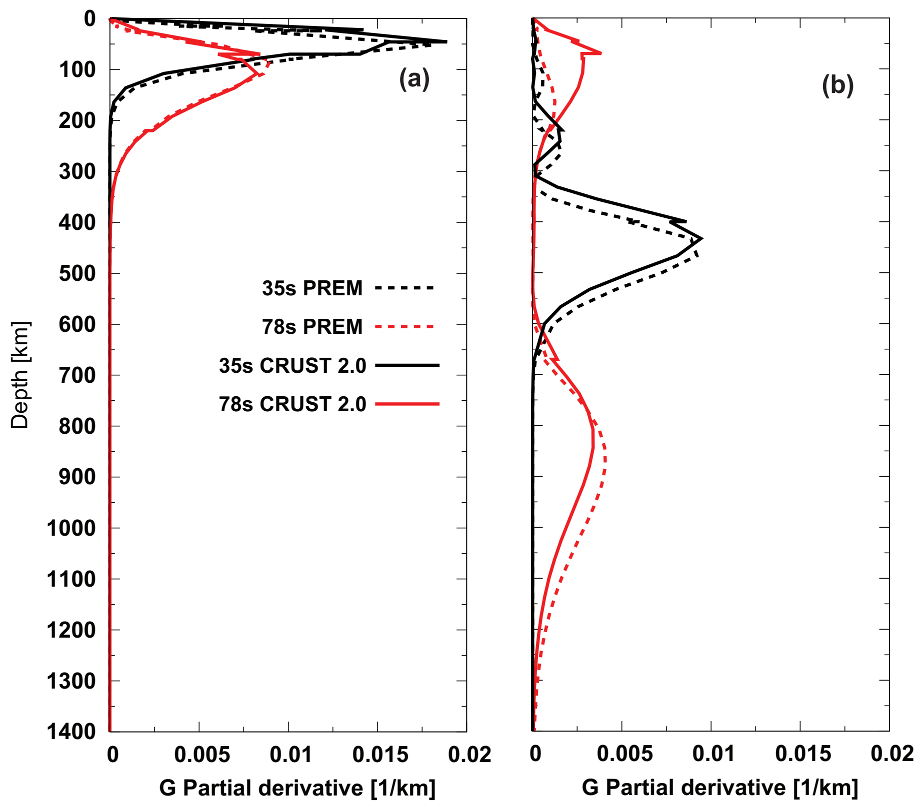

Supplementary Figure 4

Supplementary Figure 4: Effect of the crustal model on 35 s and 78 s Rayleigh wave fundamental mode (a) and third overtone (b) partial derivatives. The sensitivity kernels were calculated for relative perturbations in parameter G using PREM (dashed lines) and using a local model (solid lines) composed of PREM (Dziewonski and Anderson, 1981) and CRUST2.0 (Bassin et al., 2000).

B and H models

The average B and H models obtained are shown in Supplementary Fig. 5 for completeness. Their depth dependence closely resembles that of G, with peaks in relative amplitude between 1 and 2% at the same depths as G/L in the top 200 km, and smaller peaks (of about 7.5%) above, inside, and below the MTZ. These models should however not be taken at face value since they are affected by large trade-offs as explained below.

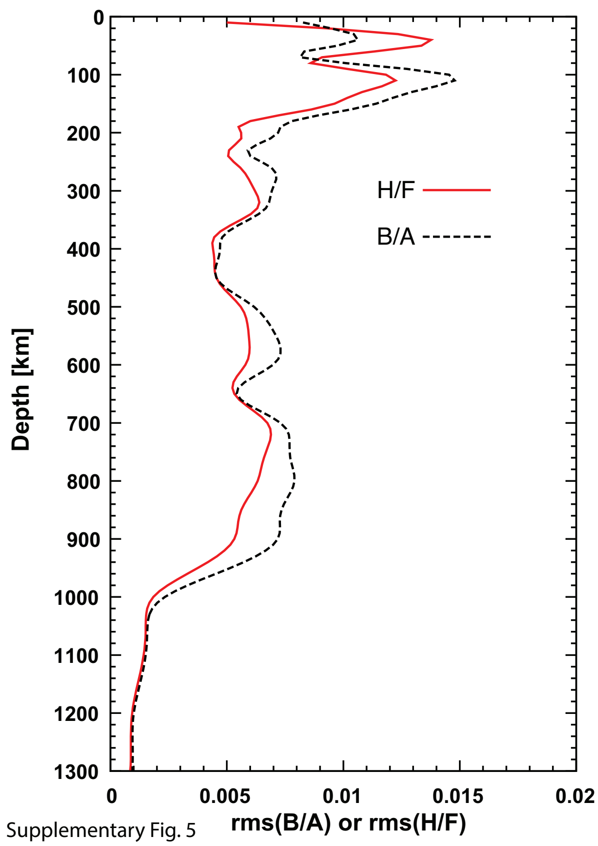

Supplementary Fig. 5

Supplementary Figure 5: Root mean square amplitude of P-wave related parameters B/A and H/F versus depth.

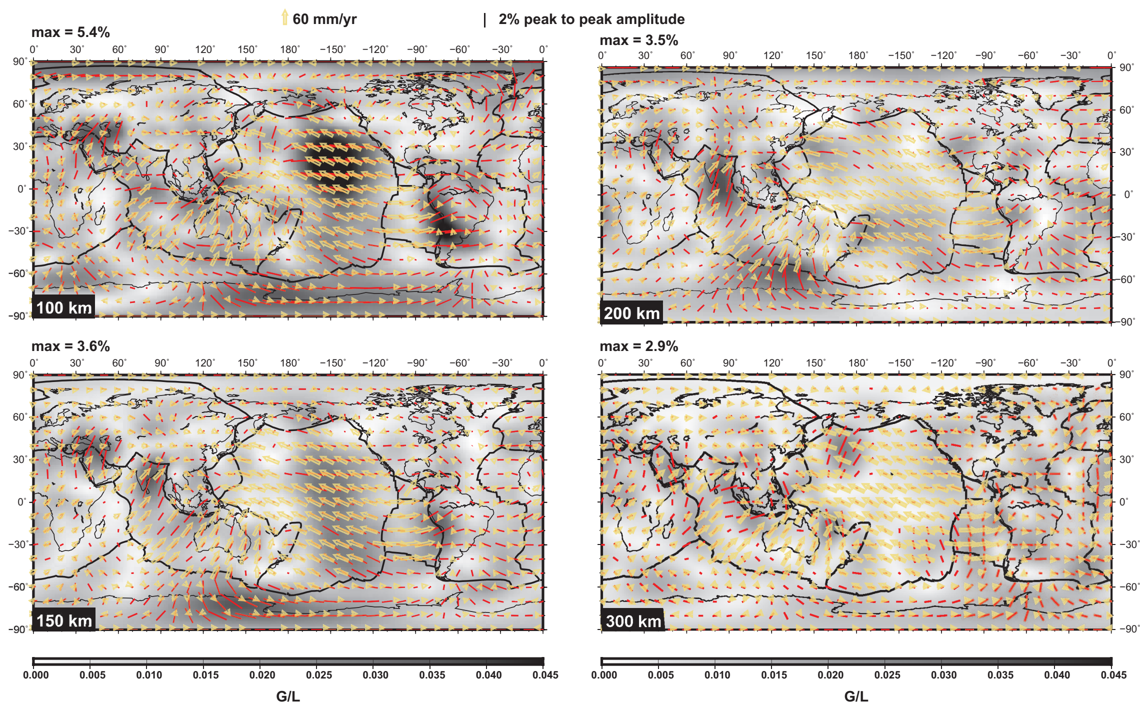

Supplementary Figure 6

Supplementary Figure 6: Global azimuthal anisotropy model superimposed onto the APM calculated using HS3-NUVEL 1A in the no-net rotation reference frame (Gripp and Gordon, 2002). The red bars represent the fast direction for vertically polarized shear-waves and their length is proportional to the anisotropy amplitude. The grey scale is also indicative of the anisotropy relative amplitude. Plate boundaries are shown by thin black lines. The maximum anisotropy amplitude is displayed on top of each panel.

Testing different APM reference frames

Supplementary Figs. 7(a) and 7(b) demonstrate that using model HS3-NUVEL 1A in the hotspot reference frame instead yields a poorer agreement between APM and fast axes than NNR-HS3-NUVEL 1A in old oceans and cratons. A slight improvement was found for the younger oceans. We also found little differences between using NNR-HS3-NUVEL 1A or model GEODVEL Argus et al. (2010) for oceans (Supplementary Fig. 7(a) and 7(c)). For cratons, the alignment is slightly better using NNR-HS3-NUVEL 1A around 250 km depth, but a second peak is well visible around 400-450 km using GEODVEL. This second peak was also present with NNR-HS3-NUVEL 1A but was much less strong. This might indicate that Θ aligns in the direction of mantle flow beneath cratons to greater depths than previously thought and possibly to greater depths than beneath oceans. Of course an anisotropy model with higher lateral resolution than ours would help investigate more reliably these differences between anisotropy below oceans and below continents at large depths. Finally, Supplementary Fig. 7(d) shows that if we isolate the Pacific plate from all other oceanic plates no difference is found between the various reference frames, and the alignment is even better than for all the oceans averaged together. This is most likely due to our limited horizontal resolution and the fact that other oceanic plates are smaller than the Pacific plate.

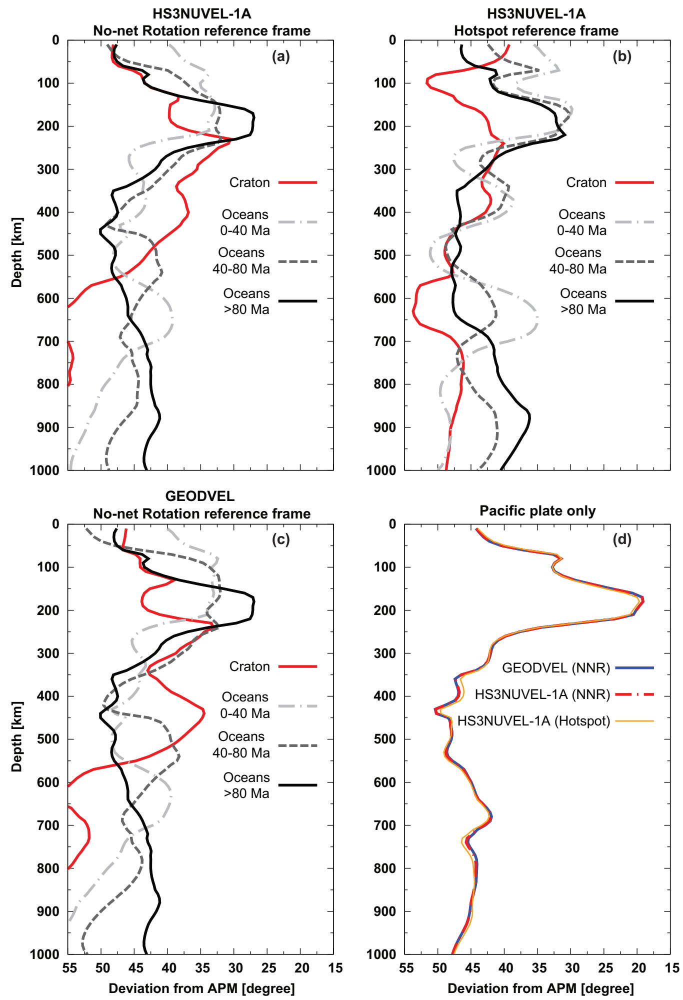

Supplementary Fig. 7

Supplementary Figure 7: Deviation between Θ and the APM calculated using model (a) HS3-NUVEL 1A in the no-net rotation reference frame, (b) HS3-NUVEL 1A in the hotspot reference frame (Gripp and Gordon, 2002), and (c) GEODVEL Argus et al. (2010) for different tectonic settings. Panel (d) shows the deviation for the Pacific plate only for all three reference frames.

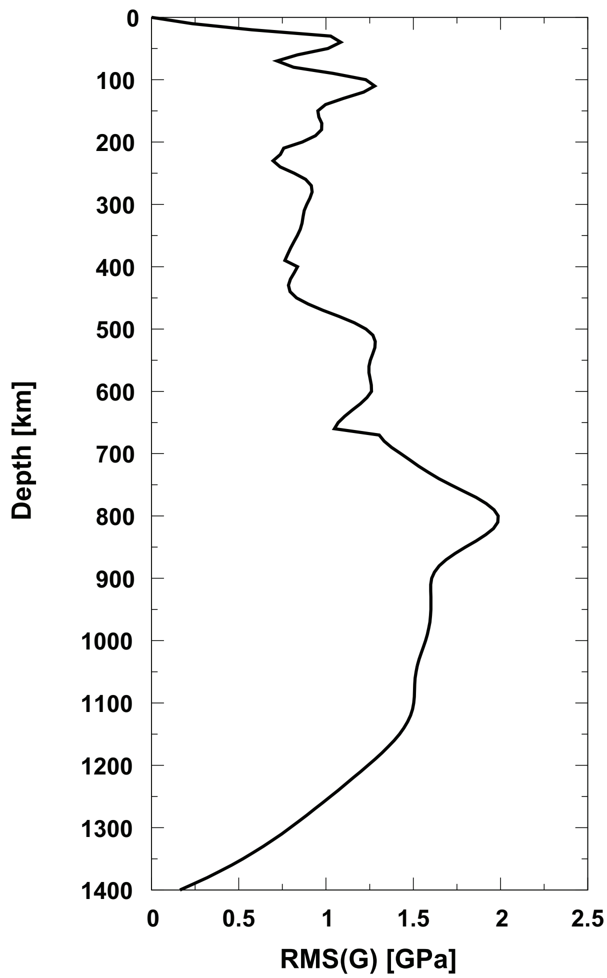

Supplementary Figure 8

Supplementary Figure 8: Root mean square amplitude for absolute parameter G versus depth.

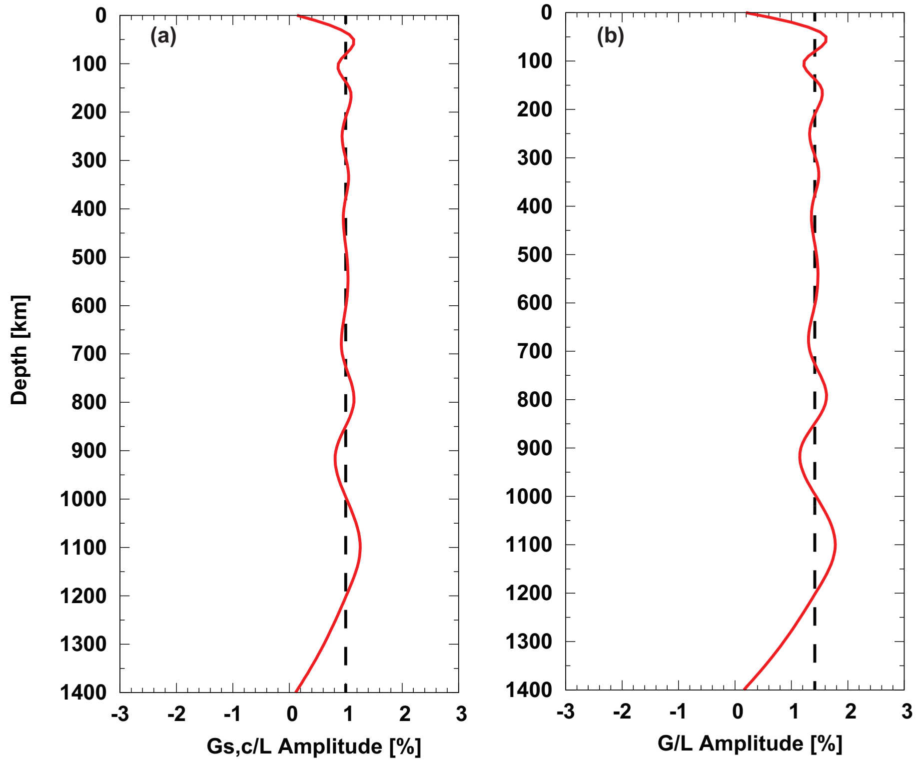

Supplementary Figure 9

Supplementary Figure 9: Synthetic tests for G_s/L and G_c/L (a), and the resulting relative amplitude G/L (b) using the damping chosen for our model. The dashed black lines represent the input model and the solid red lines represent the output

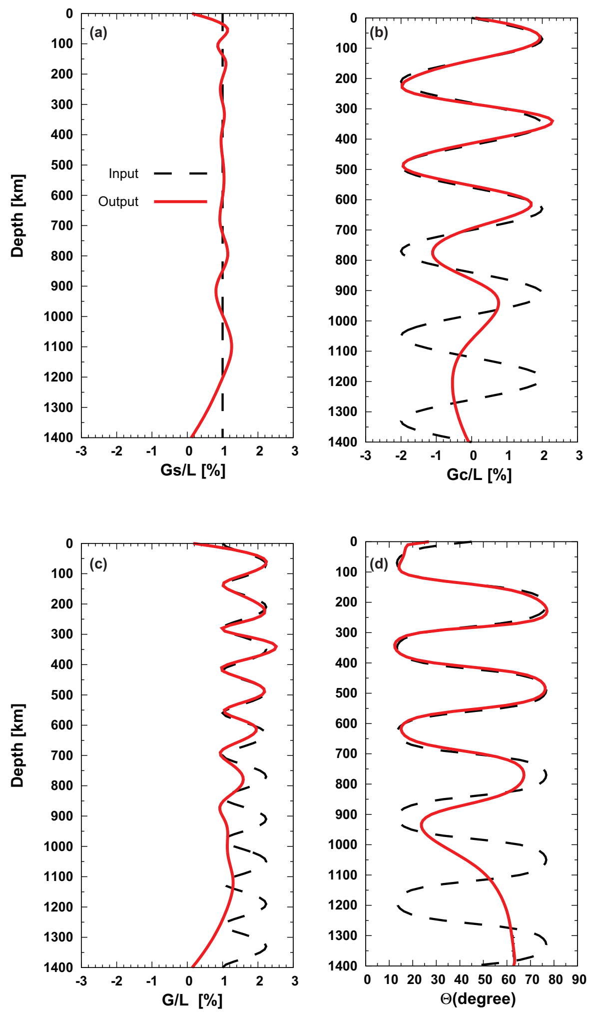

Supplementary Figure 10

Supplementary Figure 10: Synthetic tests for G_c/L (a), G_s/L (b), and the resulting amplitude G (a) and fast anisotropy axis Θ (d) using the damping chosen for our model. The dashed black lines represent the input model and the solid red lines represent the output. Layers are represented by peaks in amplitude and changes in Θ every 200 km .

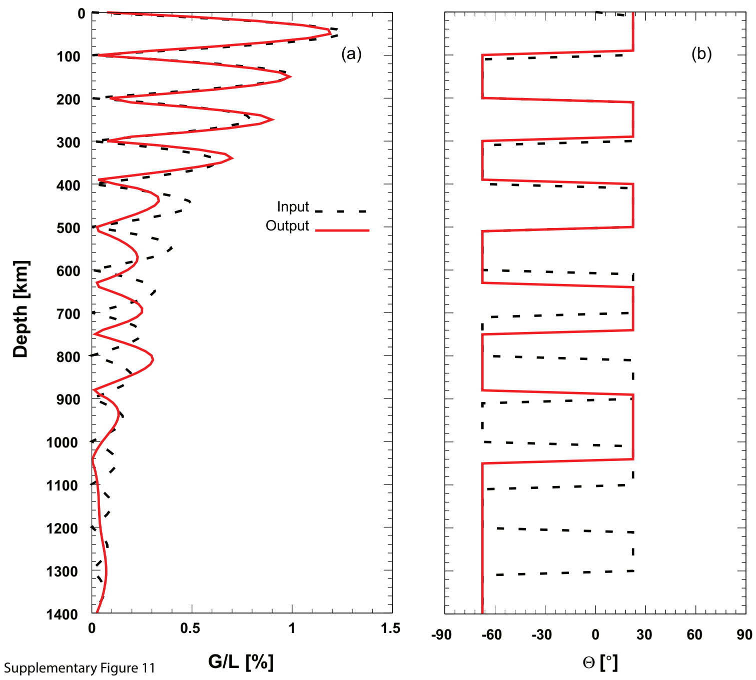

Supplementary Figure 11: Synthetic test for G/L (a) and Θ (b) using the damping chosen for our model. The dashed black lines represent the input model and the solid red lines represent the output. Layers are represented by peaks in amplitude and $90°$ changes in Θ every 100 km .

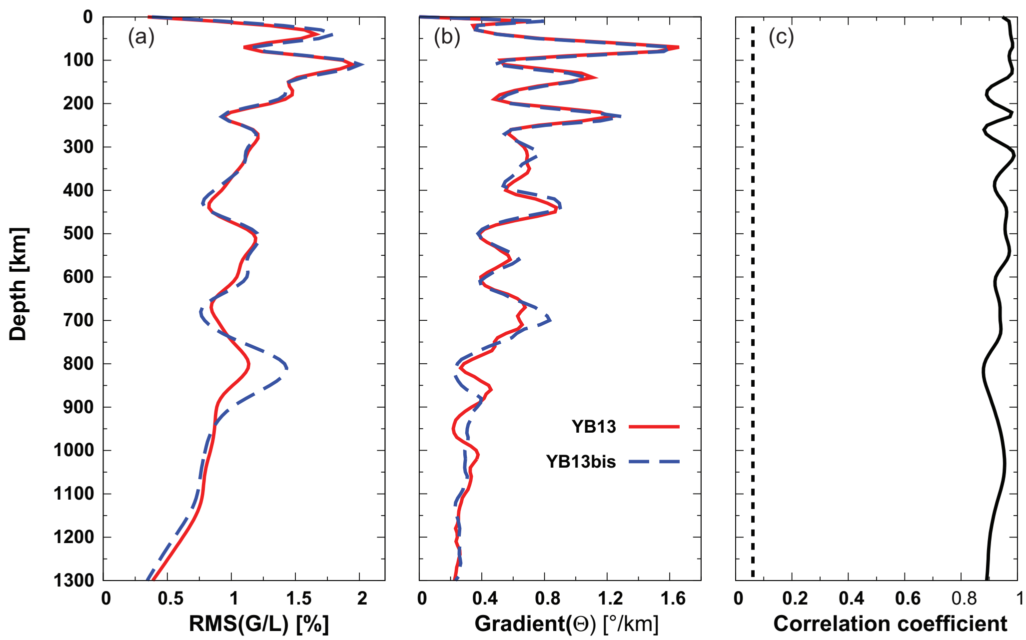

Supplementary Figure 12

Supplementary Figure 12: Comparison between model YB13 obtained while accounting for the effect of 3-D variations in crustal structure on the sensitivity kernels and model YB13bis obtained using sensitivity kernels based on PREM (Dziewonski and Anderson, 1981). (a) Rms of azimuthal anisotropy amplitude versus depth; (b) Rms of the gradient of the fast axis versus depth. Details on the calculation of the gradient are in the caption of Fig. 2 in the main manuscript; (c) Correlation coefficient between the two models versus depth and 95% significance level (vertical dashed line) calculated following Becker et al. (2007).

Effect of 3-D mantle structure

Even though 3-D mantle heterogeneities are smaller than 3-D crustal structure and thus unlikely to have a significant effect on the model, we also tested he effect of 3-D mantle heterogeneities on the kernels and resulting model for completeness. We used 3-D velocity model S40RTS (Ritsema et al., 2010) and CRUST2.0 (Bassin et al., 2000) at a grid cell located at -5° latitude and 31° longitude to calculate new local partial derivatives for G/L. We then inverted the data at that location to determine whether the amplitude minima and high $d\Theta/dr$ found at the MTZ boundaries were affected by 3-D mantle structure. Supplementary Fig. 13 shows that very little change was found in the anisotropy amplitude or in the fast anisotropy axis.

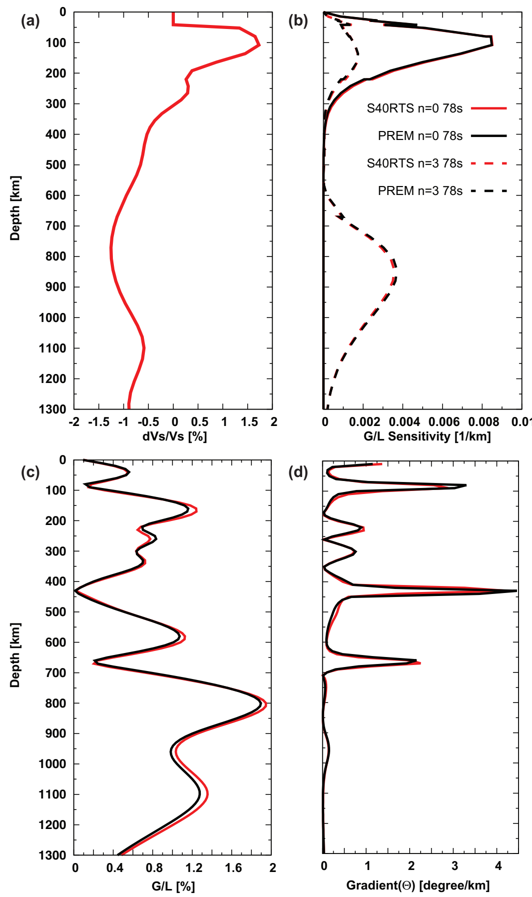

Supplementary Figure 13

Supplementary Figure 13: Effect of 3-D velocity structure. (a) Local S40RTS velocity perturbation profile (Ritsema et al., 2010); (b) Local G/L partial derivatives for fundamental modes and the third overtone Rayleigh waves at 78 s. Black lines represent partial derivatives calculated based on PREM (Dziewonski and Anderson, 1981) and CRUST2.0 (Bassin et al., 2000). Red lines correspond to curves calculated with S40RTS and CRUST2.0; (c) and (d) display the effect of 3-D velocity on anisotropy amplitude and fast axis, respectively.

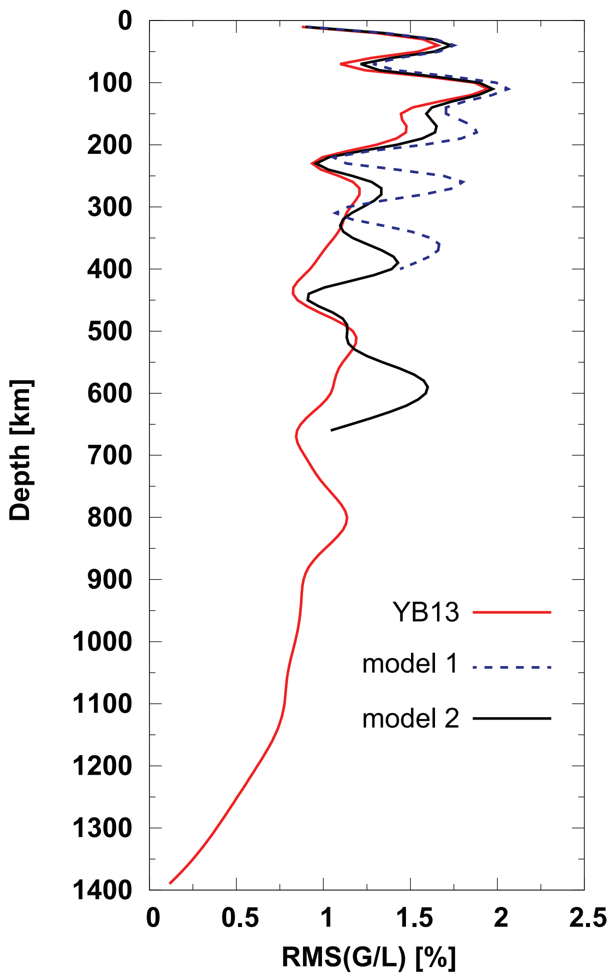

Supplementary Fig. 14

Supplementary Figure 14: Root mean square relative anisotropy amplitude for YB13 and for the two models employed in the F-test described in section 4.5. Model 1 is constructed in such a way that it has no anisotropy below 410 km and model 2 has no anisotropy below 670 km. All models were regularized and the chosen regularization compromises between data fit and model size.

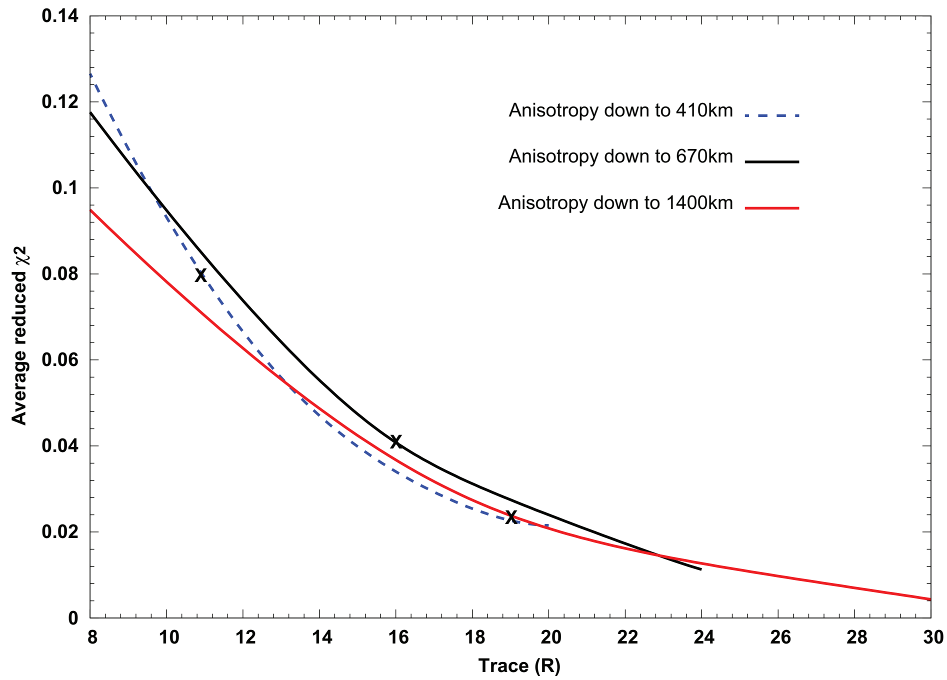

Supplementary Fig. 15

Supplementary Figure 15: Average reduced χ^2 as a function of the trace of resolution matrix, or number of independent parameters, for three types of inversions : inversions in which anisotropy is allowed down to 1400 km depth, and inversions in which anisotropy is not allowed below 410 km and 670 km. The models used in the F-tests are represented by the black crosses.

Effect of B and H

The resolution matrix shown in Supplementary Fig. 2 demonstrates that little trade-offs exist between G and the two P-wave parameters B and H. While there is no physical reason to neglect B and H in inversions for azimuthal anisotropy, this assumption is often done in similar studies for mathematical convenience. One might therefore wonder whether our results are stable if we neglect B and H in our inversions.

Synthetic tests were first performed to assess the effect of B and H on the G model. We found (Supplementary Fig. 16) that for an input model in which $B = H = 0$, the output G model is not significantly affected by the introduction of the P-wave parameters in the inversion, and that an inversion for all three parameters yields B and H that are close to the input. For an input model that has non-zero B, H, and G (Supplementary Fig. 17) we cannot retrieve B and H reliably, but the output G model is closer to the input when B and H are included in the inversion. This shows that overall inversions for all three parameters should be preferred over inversions for G only.

For completeness, we nevertheless performed a new set of inversions in which we assumed $B = H = 0$. Supplementary Fig. 18 compares the results of this new inversion, thereafter referred to as model YB13-G, with model YB13. The rms amplitude peaks at similar depths in both models. However, the amplitude of the anisotropy in YB13-G is significantly larger below 300 km depth. Similarly, the vertical gradient of the fast axes does not change much in the top 300 km, but becomes weaker at larger depths. We still find peaks in the vertical gradient at the MTZ boundaries, but they are less strong than in YB13. Calculations of VR for the two models also showed that model YB13 explains 86 % of the data whereas model YB13-G explains only 65 % of the data. We additionally conducted F-tests to compare the reduced χ^2 misfit of the two models (Supplementary Fig. 19). This test showed that the lower χ^2 misfit of YB13 is significant, and that the probability that the data require the P-wave anisotropy parameters to be included in the inversions is at least 99 % at most locations.

Despite some differences between our G model and that obtained when neglecting the P-wave parameters (Supplementary Fig. 18), we thus conclude that that there is no reason to neglect B and H, and that our results are reliable.

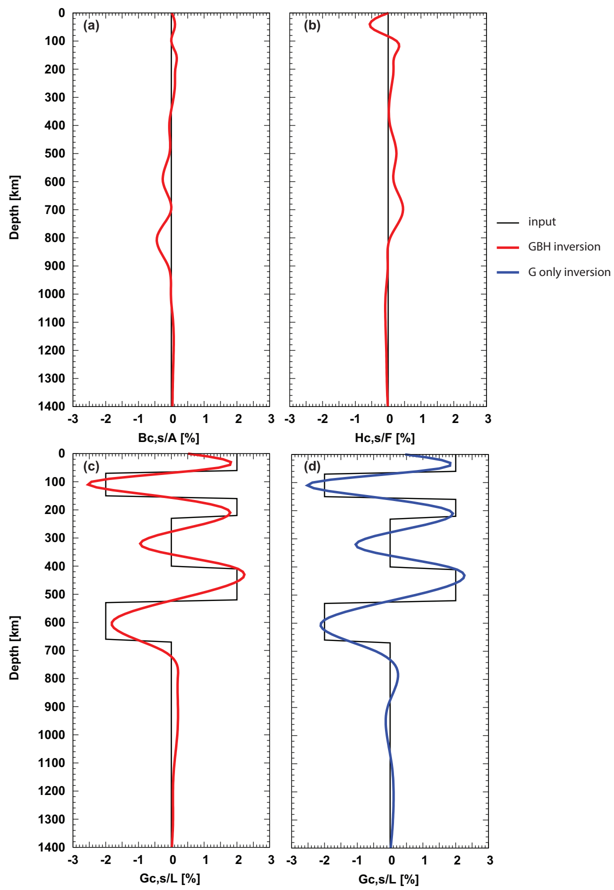

Supplementary Fig. 16

Supplementary Figure 16: Synthetic tests with input models characterized by $B = 0$ (a) and $H = 0$ (b). The input G model is shown in (c) and (d) together with the output G in two different inversion cases described above. The output models in (a), (b), and (c) were obtained by inverting the synthetic data for all three elastic parameters. The output model in (d) was obtained by inverting synthetic data for G only.

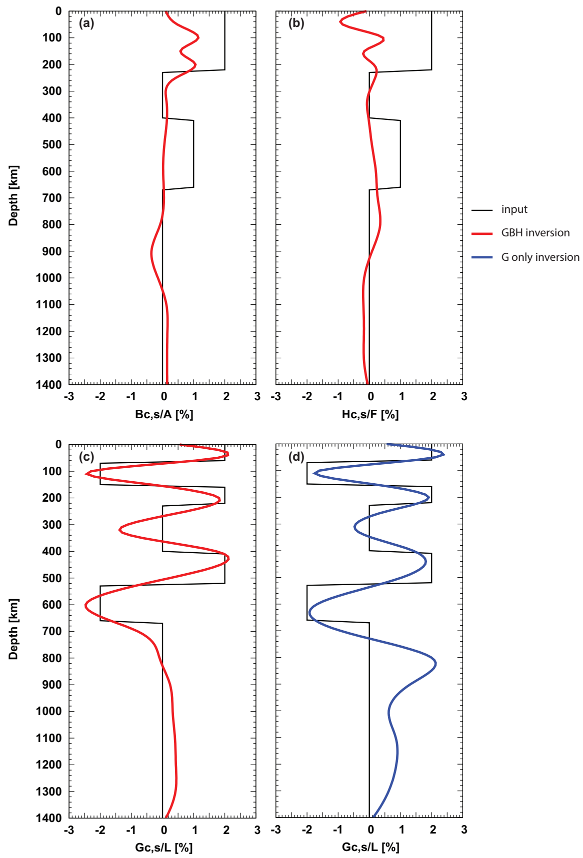

Supplementary Fig. 17

Supplementary Figure 17: Synthetic tests with input models characterized by non-zero B (a) and H (b). The input G model is shown in (c) and (d) together with the output G in two different inversion cases. The output models in (a), (b), and (c) were obtained by inverting the synthetic data for all three elastic parameters. The output model in (d) was obtained by inverting the synthetic data for G only.

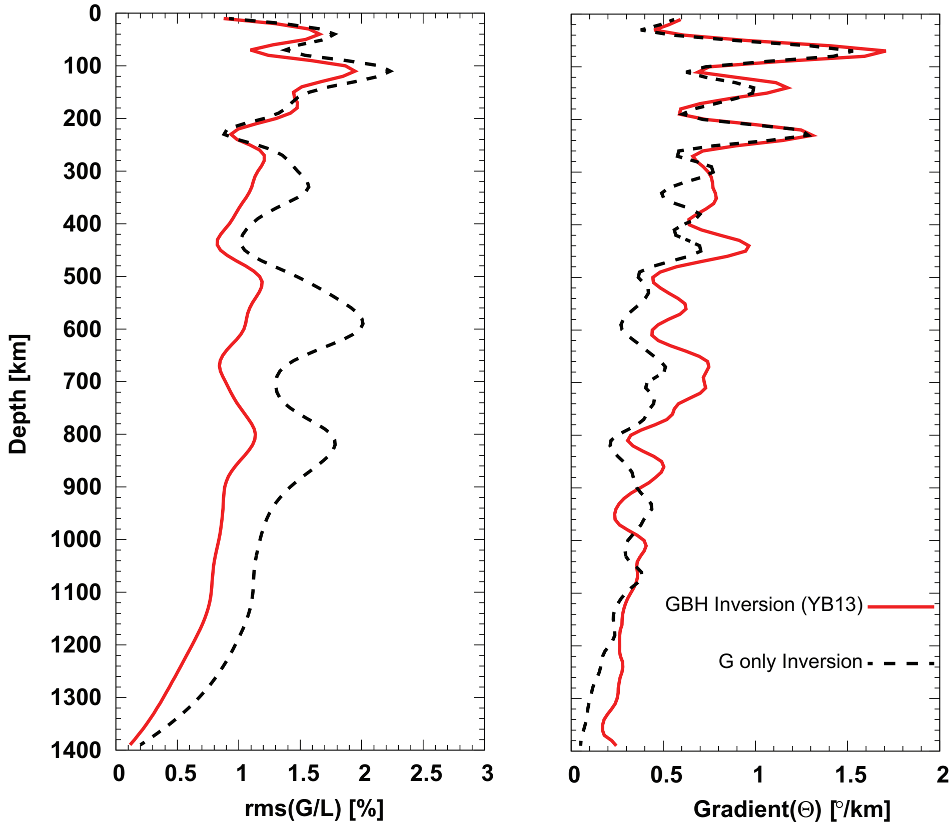

Supplementary Fig. 18

167 **Supplementary Figure 18**: Root mean square amplitude (a) and ver-
168 tical gradient of the fast axes (b) for model YB13 and a model obtained by
169 inverting for G only.

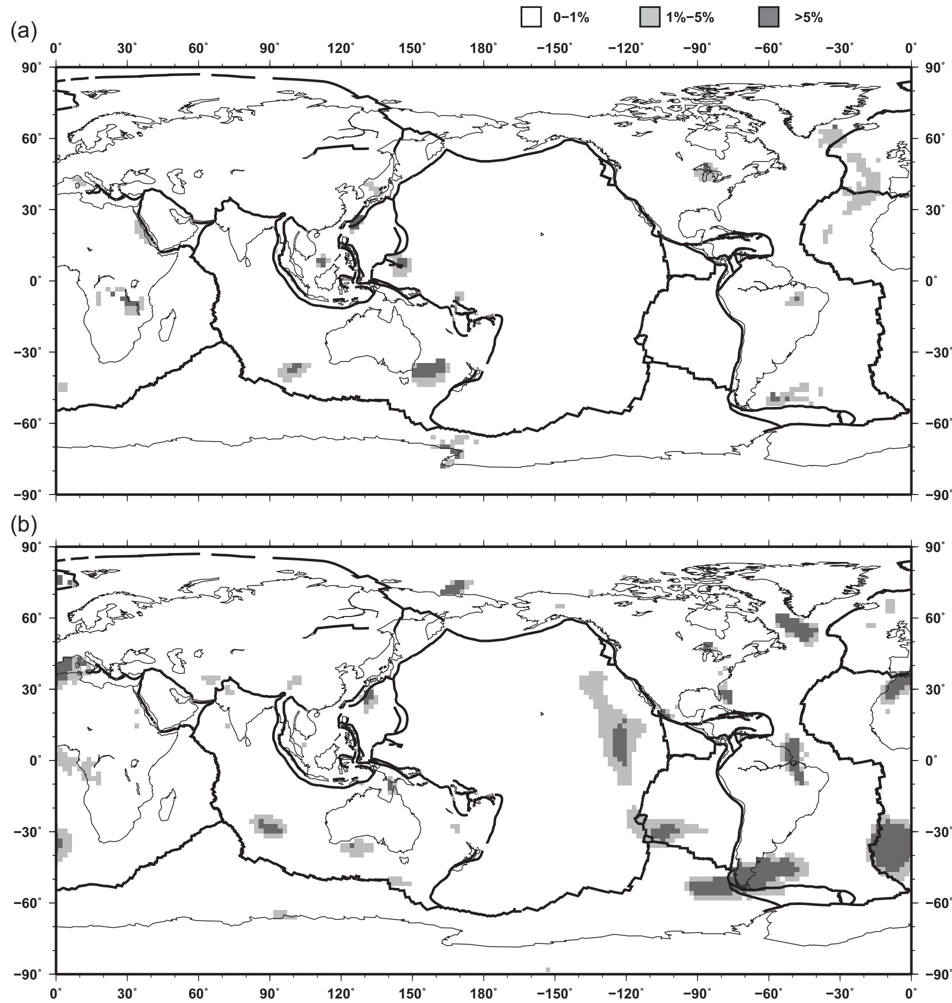

Supplementary Fig. 19

Supplementary Figure 19: Statistical F-tests conducted for Gc (a) and G_s (b) to compare model YB13 with a model obtained by inverting for G only. The color scale represents the probability that the two models are equivalent.

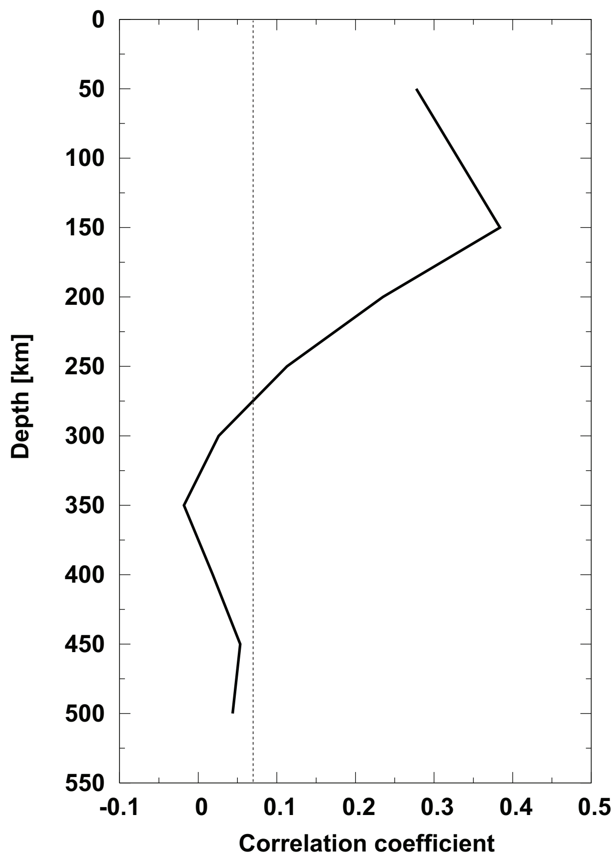

Supplementary Fig. 20

Supplementary Figure 20: Global correlation between our model and the anisotropy of model DPK2005 (Debayle et al., 2005) calculated following Becker et al. (2007). The 95 % significance level for a degree 20 expansion is denoted by the vertical dashed line.

References

Argus, D. F., Gordon, R. G., Heflin, M. B., Ma, C., Eanes, R. J., Willis, P., Peltier, W. R., Owen, S. E., 2010. The angular velocities of the plates and the velocity of Earth's centre from space geodesy. Geophysical Journal International 180 (3), 913–960.

Bassin, C., Laske, G., Masters, G., 2000. The current limits of resolution for surface wave tomography in north america. In: EOS Trans AGU. Vol. 81.

Becker, T. W., Ekström, G., Boschi, L., Woodhouse, J. H., 2007. Length scales, patterns and origin of azimuthal seismic anisotropy in the upper mantle as mapped by Rayleigh waves. Geophysical Journal International 171, 451–462.

Debayle, E., Kennett, B., Priestley, K., 2005. Global azimuthal seismic anisotropy and the unique plate-motion deformation of Australia. Nature 433 (7025), 509–512.

Dziewonski, A. M., Anderson, D. L., 1981. Preliminary reference Earth model. Physics of the Earth and Planetary Interiors 25 (4), 297—356.

Gripp, A. E., Gordon, R. G., 2002. Young tracks of hotspots and current plate velocities. Geophysical Journal International 150 (2), 321–361.

Ritsema, J., Deuss, A., van Heijst, H. J., Woodhouse, J. H., 2010. S40RTS: a degree 40 shear-velocity model for the mantle from new Rayleigh wave dispersion, teleseismic traveltime and normalmode splitting function measurements. Geophysical Journal International 184 (3), 1223–1236.